



Co-production of hydrogen and carbon nanotubes from cracking of waste cooking oil model compound over Pt–Ni/SBA-15 catalysts

Wei Liu¹ · Guoliang Zhang¹ · Songyuan Hao¹ · Hong Yuan^{1,2} · Weidong He¹

Accepted: 18 August 2021 / Published online: 28 August 2021

© The Author(s), under exclusive licence to Springer Science+Business Media, LLC, part of Springer Nature 2021

Abstract

Waste cooking oils (WCOs) are a cheap and rich source of carbon and hydrogen, and they exhibit great potential for the preparation of hydrogen gas and carbon nanomaterials. Here, we prepared three Pt–Ni/SBA-15 catalysts with Pt contents ranging from 0 to 2% to examine their activity in the catalytic cracking of WCO towards the production of hydrogen and carbon nanotubes (CNTs). A mixture of soybean oil, oleic acid and animal fat was used as a model compound of WCO, and the catalysts were characterised by inductively coupled plasma–optical emission spectrometry, scanning and transmission electron microscopy, X-ray diffraction, N₂ adsorption–desorption isotherms, temperature programmed reduction, thermogravimetric analysis and Raman spectroscopy. The effect of Pt loading and cracking temperature on the hydrogen production and the quality of CNTs was also evaluated. Among the prepared catalysts, 2%Pt–30%Ni/SBA-15 showed excellent catalytic activity at 750 °C, affording a maximum hydrogen content of 66.2 vol%, while CNTs with diameters of 20–100 nm and high crystallinity, oxidation stability, graphitisation and purity were also prepared.

Keywords Waste cooking oil · Catalytic cracking · Pt–Ni bimetal · Hydrogen production · Carbon nanotubes

1 Introduction

Hydrogen (H₂) is considered a clean and efficient energy carrier, as no carbon oxides (CO_x) are emitted during combustion. Moreover, H₂ demonstrates the highest specific energy

(140 MJ kg⁻¹) among all actual fuels, which is also more than twice as high as typical solid fuels [1]. Therefore, due to its high calorific value of combustion and non-polluting combustion characteristics, H₂ is expected to be used for the development of alternative fuel systems to reduce our dependence on fossil fuels.

Photocatalytic water splitting on semiconductor catalysts has also been reported as a clean, sustainable and promising technology for H₂ production [2]. However, the photocatalytic H₂ production method still suffers from low conversion efficiency and high requirements for catalytic materials [3]. Furthermore, the catalytic decomposition of methane for hydrogen production has attracted great interest from researchers due to the high value-added carbon nanomaterials produced by the reaction process at the same time [4].

WCO is a kind of biomass renewable raw material, which mainly contains fatty acid triglyceride and free fatty acid. Like methane, WCO contains a large amount of carbon, hydrogen elements and a small amount of oxygen elements, in the process of cracking will produce a large amount of hydrogen. The ratio of carbon to hydrogen of WCO is about 2, which is slight lower than that of methane, but obviously higher than that of ethanol. Zhou et al. studied the effect of temperature and a Fe₃O₄ catalyst on

Wei Liu and Guoliang Zhang have contributed equally to this work.

✉ Hong Yuan
yuanhong@nun.edu.cn

Wei Liu
343118432@qq.com

Guoliang Zhang
1143705245@qq.com

Songyuan Hao
813490032@qq.com

Weidong He
2753231274@qq.com

¹ School of Chemistry and Chemical Engineering, North Minzu University, Yinchuan 750021, China

² State Key Laboratory of National Ethnic Affairs Commission Chemical Technology, North Minzu University, Yinchuan 750021, China

the H₂ production during WCO cracking, and they demonstrated that the use of a catalyst led to a higher H₂ conversion rate compared to the catalyst-free pyrolysis at the same reaction temperature [5].

Although very few reports are currently available for catalysts involved in the catalytic cracking of WCO, but reports using methane and ethanol as cracking raw materials show that different types of carriers and active metals have been used in cracking reactions. In particular, when the raw material should be completely cracked or gasified at > 600 °C, materials with high temperature resistance, such as SBA-15, Al₂O₃, MgO, MgO·Al₂O₃, ZrO₂, MCM-41 and carbon, can be selected as catalysts supports. Among them, SBA-15 is a stable at high temperatures and exhibits regular and orderly mesoporous channels. Nickel (Ni) also attracted particular attention as active metal due to its high activity in cracking reactions compared to other metals. However, Ni-based catalysts can rapidly lose their activity at temperatures above 600 °C.

Cost-effective bimetallic catalysts with excellent performance and high catalytic efficiency can be prepared by modifying monometallic catalysts with a small amount of precious metals. For example, Ni/CeO₂ and Pt-promoted Ni/CeO₂ catalysts have been applied to H₂ production, indicating that the H₂ yield of CH₄ cracking could be improved by adding 0.2% Pt [6]. At 700 °C, the maximum H₂ yield of Ni/CeO₂ was 46% and that of Pt-promoted Ni/CeO₂ was 54%. Monometallic Ni/SBA-15 and Pd-promoted Ni/SBA-15 catalysts have also been prepared and applied to CH₄ decomposition [7]. Ni/SBA-15 exhibited lower activity than the Pd-promoted Ni/SBA-15 catalyst, because after the first 180 min, the activity of Ni/SBA-15 gradually decreased, and only 46% H₂ yield was achieved. In contrast, the addition of 0.2% and 0.4% Pd increased the yield to 48% and 59%, respectively. In addition, the addition of a small Pt amount (0.1%) to Ni/MgAl₂O₄ catalysts led to a maximum CH₄ conversion rate of 14% at 700 °C and promoted the formation of CNTs from CH₄ [8].

In our previous study [9], the Ni-Co/SBA-15 catalyst was synthesized for the catalytic cracking of waste cooking oil model compound. Although a maximum hydrogen content of 71.5 vol% could be obtained by using 20%Ni-30Co%/SBA-15 catalyst at 750 °C, however, the total metal content of Ni and Co was too high, resulting to pore plugging of SBA-15. It was not conducive to the diffusion of reactants in the pores. In addition, the high total metal content also led to the higher cost of catalyst. In current study, Pt–Ni/SBA-15 bimetallic catalyst was synthesized by doping a small amount of Pt into Ni-based catalyst to explore the promoting effect of noble metals on Ni-based catalysts under different cracking conditions. In addition, we examined in detail the high value-added carbon nanomaterials deposited on the catalyst surface during the cracking process.

2 Experimental part

2.1 Materials

The PEO–PPO–PEO triblock copolymer [PEO: poly(ethylene oxide); PPO: poly(propylene oxide)] was supplied by Sigma–Aldrich. Hydrochloric acid (36%) was purchased from Sinopharm Chemical Reagent Co., Ltd, while tetraethyl orthosilicate (TEOS, 98%), nickel nitrate hexahydrate [(Ni(NO₃)₂·6H₂O) (99%), chloroplatinic acid solution (PtH₂Cl₆·6H₂O) (Pt ≥ 37.5%), soybean oil and oleic acid were supplied by Aladdin. Animal fat was purchased from the local market.

2.2 Preparation of WCOMC

The WCOMC was prepared according to our previous study [9]. In brief, soybean oil [saponification value (SV) = 189 mg KOH g⁻¹, acid value (AV) = 4 mg KOH g⁻¹, average molecular weight (MW) = 910] and animal fat (SV = 210 mg KOH g⁻¹, AV = 3 mg KOH g⁻¹, average MW = 813) with a mass ratio of 18:1 were heated and stirred at 150 °C for 6 h. Then, oleic acid was added using the same mass as the animal fat, and the WCOMC used in this study as raw material was obtained.

2.3 Preparation of SBA-15

The catalyst support, SBA-15, was prepared by the hydrothermal method based on a previous study [10]. First, 4.0 g of P123 [(EO)₂₀(PO)₇₀(EO)₂₀, MW = 5800] was dissolved upon stirring in 120 g of a 2 mol L⁻¹ hydrochloric acid solution. Then, TEOS (8.5 g) and deionised water (30 g) were sequentially added, and the mixture was stirred at 40 °C for 24 h. Afterward, the mixture was hydrothermally treated at 100 °C for 48 h and dried at 90 °C for 12 h. The dried sample was finally calcined in air at 550 °C (heating rate of 1 °C min⁻¹) for 6 h, and the template(P123) was removed to obtain SBA-15.

2.4 Synthesis of Ni-based catalysts

Ni(NO₃)₂·6H₂O (1.485 g) was dissolved in 450 mL deionised water, and PtH₂Cl₆·6H₂O (0.03862 mol L⁻¹, 2.656 mL) and SBA-15 (0.68 g) were added. The mixture was magnetically heated and stirred at 85 °C until the mixture evaporated into a uniform paste. Then, the paste was transferred to an evaporating dish and dried at 100 °C for 12 h. Afterward, to obtain the 2%Pt–30%Ni/SBA-15 catalyst (1.0 g), the resulting solid was calcined in the air at 500 °C at a heating rate of 3 °C min⁻¹ for 5 h. The amount of Pt was set at 1 and 2

wt% by adjusting the amount of the Pt precursor and SBA-15. 30%Ni/SBA-15 was prepared following the same process without the addition of $\text{PtH}_2\text{Cl}_6 \cdot 6\text{H}_2\text{O}$.

2.5 Cracking apparatus and procedure

The composition of the reaction system, the catalyst reduction steps and the liquid feeding process has been reported in our previous study [9]. In brief, 1.0 g of the catalyst was filled into the centre of the reaction tube, and the temperature was raised to 650 °C under N_2 flow (40 mL min^{-1}). Then, the atmosphere was changed from N_2 to H_2 (40 mL min^{-1}), and the catalyst was reduced at the same temperature for 2 h. Afterward, to completely remove the residual H_2 in the reactor, the atmosphere was changed again to N_2 (30 mL min^{-1}) for 1 h. Then, the reaction system was heated to the predetermined reaction temperature, and the WCOMC, already heated to 80 °C, was added to the reactor using N_2 at a feed rate of 0.02 mL min^{-1} .

The instantaneous concentration of each gas product was detected and recorded by a GC-7820 gas chromatograph equipped with a 5A packed column, a TDX-01 packed column, a natural gas special packed column, a H_2 flame ionisation detector and a thermal conductivity detector. The concentration of each gas component flowing through the detector was recorded as an electrical signal, and the instantaneous volume fraction of each component was calculated using the gas outflow and standard curves. After detection, each gas was directly vented. The content of a gas component was calculated according to the equation:

$$\text{Content}_i \text{ (vol\%)} = \left(\frac{n_i}{n_{\text{tot}}} \right) \times 100, \quad (1)$$

where n_i (vol%) is the instantaneous volume fraction of component I , and n_{tot} (vol%) represents the sum of the instantaneous volume fractions of all gas components. Moreover, the carbon yield was calculated using the formula:

$$\text{Carbon yield \%} = \frac{\% \text{ weight loss by carbon oxidation}}{\% \text{ of residue after oxidation}} \times 100 \quad (2)$$

2.6 Characterisation

The Pt and Ni content in the prepared catalysts was determined by inductively coupled plasma–optical emission spectrometry (ICP–OES) using a 730 Series spectrometer (Agilent Technologies, Santa Clara, CA, USA). The X-ray diffraction (XRD) patterns of the fresh and spent catalysts were recorded on a SmartLab diffractometer (Rigaku, Japan) with $\text{Cu-K}\alpha$ radiation operating at 40 kV and 30 mA. The textural properties of the catalysts were studied using a

specific surface area and porosity analyser at 77 K (ASAP 2020, Micrometrics Instrument Corp., Norcross, GA, USA). Before analysis, all catalysts were degassed at 200 °C for 5 h. The external morphology and oxide particle size of SBA-15 and the catalysts were studied by field emission scanning electron microscopy (FESEM; Gemini 500, Carl Zeiss Microscopy GmbH, Jena, Germany). Next, transition electron microscopic (TEM) analysis of the catalysts and CNTs was performed on a Tecnai G2 F20 instrument (FEI, Hillsboro, OR, USA) with an accelerating voltage of 200 kV. The reducibility of the fresh catalysts was studied by H_2 -temperature programmed reduction (H_2 -TPR) on a chemical adsorption analyser (AutoChem II 2920, Micrometrics Instrument Corp., Norcross, GA, USA).

The morphological appearance of the deposited CNTs was studied using a SEM tungsten filament (EVO 18, Carl Zeiss Microscopy GmbH, Jena, Germany). The thermal stability and carbon yield of CNTs were studied by thermogravimetric analysis (TGA) on a thermal analyser (STA 449 F5, Netzsch-Gerätebau GmbH, Selb, Germany). The oxidation temperature increased from 50 to 850 °C in the air. The Raman spectra were recorded on a Renishaw System 2000 spectrometer (Renishaw Inc., West Dundee, IL, USA).

3 Results and discussion

3.1 ICP–OES analysis of the Ni-based catalysts

The actual amount of Pt and Ni in the prepared catalysts were determined by ICP–OES analysis. As shown in Table 1, the actual amount of Pt and Ni were lower than that of the theoretical values.

3.2 XRD analysis

To analyse and identify the phase and material structure of the support and the catalysts, XRD studies were also performed. Specifically, a broad peak at a 2θ range of 15° – 30° was detected in the XRD pattern of SBA-15 (Fig. 1), which was related to the typical amorphous structure of this catalyst support [11]. In contrast, this peak was almost flattened in the XRD patterns of all Ni-based catalysts, indicating

Table 1 Pt and Ni contents in the prepared catalysts

Catalyst	Pt (wt%)	Ni (wt%)	Total metal content (wt%)
30%Ni/SBA-15	–	27.56	27.56
1%Pt–30%Ni/SBA-15	0.86	26.87	27.73
2%Pt–30%Ni/SBA-15	1.63	27.24	28.87

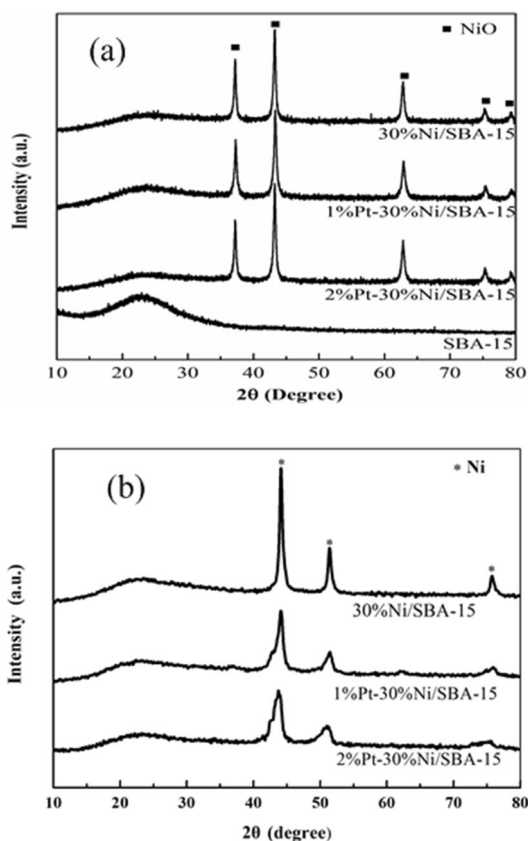


Fig. 1 Wide-angle XRD patterns of the **a** calcined catalysts, **b** catalysts being reduced with H₂

that the supported metals affected the structure of SBA-15. In addition, the diffraction peaks detected at 37.2°, 43.2°, 62.9°, 75.3° and 79.5° were attributed to the existence of a NiO phase with a face-centred cubic structure. However, no diffraction peaks related to PtO₂ were observed after the Pt addition, suggesting that the PtO₂ particles were well dispersed on the catalyst surface. This result further supported our SEM results that a small amount of noble metals can improve the dispersibility of metal particles.

The XRD pattern of reduced catalysts are shown in Fig. 1b. No diffraction peaks of NiO appeared, suggesting that NiO was completely reduced to Ni. In addition, no diffraction peaks related to Pt were still observed, indicating that the Pt particles were well dispersed on the catalyst surface.

3.3 N₂ adsorption–desorption analysis

The pore structure characteristics and specific surface area of SBA-15 and the Ni/SBA-15 and Pt–Ni/SBA-15 catalysts were analysed by the Brunauer–Emmett–Teller (BET) method. As shown in Fig. 2a, all catalysts exhibited type-IV N₂ adsorption–desorption isotherms [12] with typical H1

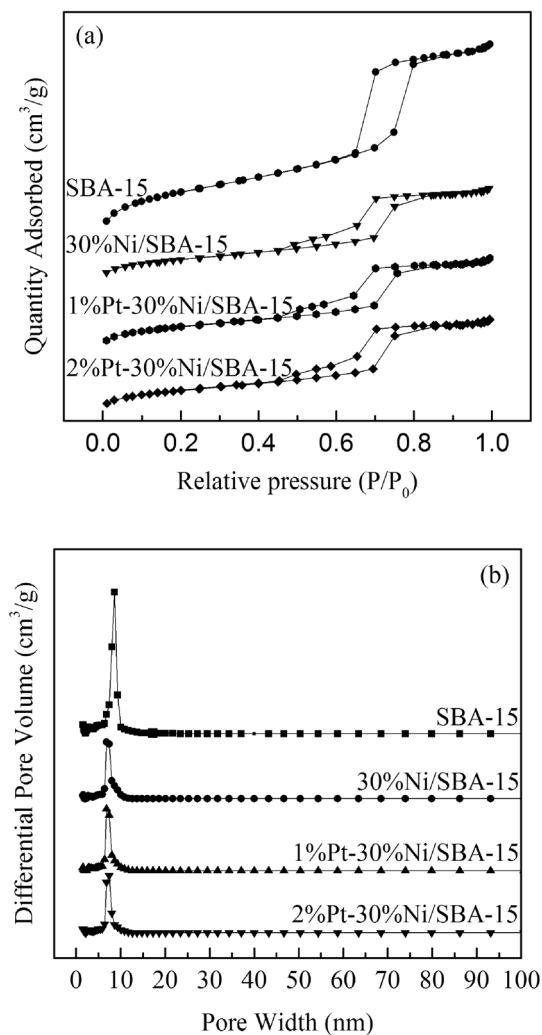


Fig. 2 N₂ adsorption–desorption isotherms and pore size distribution of SBA-15 and the prepared catalysts

hysteresis loops. More specifically, the hysteresis loop of SBA-15 was observed in a relative pressure (P/P_0) range of 0.6–0.9 and occupied a large area. However, after Ni and Pt loading, due to the structural change caused to the support by the added metals, flatter hysteresis loops that shifted to lower relative pressure values ($P/P_0 = 0.4–0.9$) were observed compared to SBA-15. In addition, both SBA-15 and the prepared catalysts exhibited a uniform pore size distribution (Fig. 2b). The pore sizes of SBA-15 were mainly concentrated between 5 and 10 nm, indicating that the structure of the catalyst support was mainly mesoporous. However, the addition of Ni and Pt significantly reduced the number of 5–10 nm pores, although the pore size distribution was not greatly affected.

Furthermore, among the tested materials, SBA-15 exhibited the largest specific surface area, which was reduced after the addition of Ni (Table 2), probably due to the blockage of the support pore channel by NiO. Interestingly, the addition

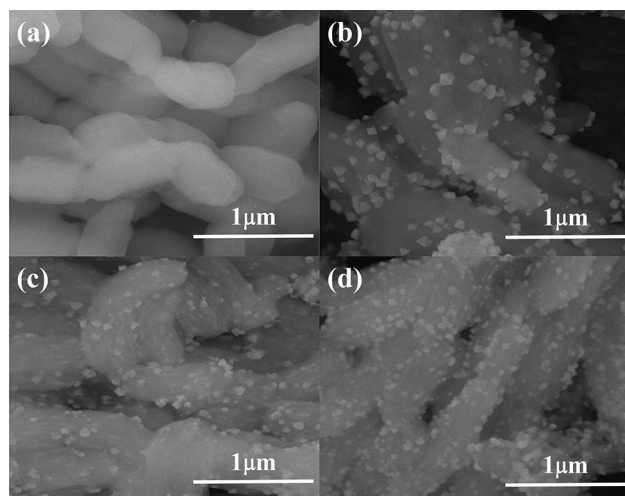
Table 2 BET surface area and porosity characteristics of SBA-15 and the prepared Ni-based catalysts

Samples	BET surface area (m ² g ⁻¹)	Pore volume (cm ³ g ⁻¹)	Pore diameter (nm)
SBA-15	861	1.225	5.7
30%Ni/SBA-15	398	0.577	5.85
1%Pt–30%Ni/SBA-15	400	0.582	5.80
2%Pt–30%Ni/SBA-15	417	0.583	5.54

of Pt increased the specific surface area and pore volume of the corresponding catalysts, and the highest values were observed for 2%Pt–30%Ni/SBA-15. These results were attributed to the synergistic effect of Pt and Ni, which was stronger as the Pt content increased and improved the dispersion of metal particles on the catalyst support [6, 13].

3.4 SEM analysis of SBA-15 and the Ni-based catalysts

The external morphology of SBA-15 and the prepared Ni-based catalysts was examined by the SEM method. SBA-15 exhibited a smooth surface and a rod-shaped structure (Fig. 3a), while the similar morphology of the Ni-based catalysts suggested that the metal loading did not significantly affect the catalyst support's morphology (Fig. 3b–d). Moreover, dispersed metal particles and no agglomeration were observed on the surface of SBA-15, irrespective of the metal content. However, the degree of metal dispersion and the size of the metal particles on the surface of 1%Pt–30%Ni/SBA-15 and 2%Pt–30%Ni/SBA-15 was more uniform than that on the surface of 30%Ni/SBA-15. This

**Fig. 3** SEM images of **a** SBA-15, **b** 30%Ni/SBA-15, **c** 1%Pt–30%Ni/SBA-15 and **d** 2%Pt–30%Ni/SBA-15

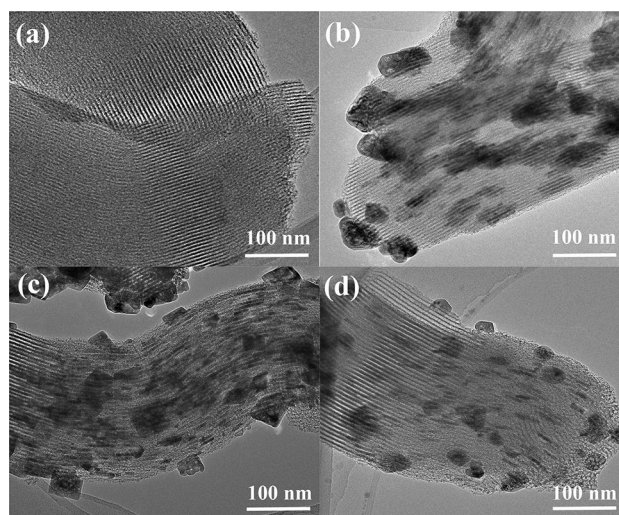
could be attributed to the addition of noble metals, which can enhance the synergy between bimetals, thereby improving the dispersibility of metal particles [14].

3.5 TEM analysis of SBA-15 and the Ni-based catalysts

TEM analysis of the internal structure of SBA-15 indicated that the catalyst support consisted of highly ordered mesoporous channels (Fig. 4a). After metal loading, unevenly distributed, non-agglomerated metal oxide particles could be observed above and inside the SBA-15 pores (Fig. 4b–d). Pt–Ni octahedral structure oxide may be formed. The sides and corners of the octahedron were formed before the surface. After the Pt–Ni concave octahedron was completely formed, Ni adhered to the surface of the Pt–Ni concave octahedron to form a complete octahedral structure [15]. Moreover, the average particle size of the metal particles of the catalyst was 68 nm, 52 nm and 38 nm, respectively (Fig. 4b–d), and the particle size of the metal particles decreased with the increase of Pt content, which was consistent with the XRD characterization result. With 2%Pt–30%Ni/SBA-15 showing the smallest particle size and a more uniform distribution compared to the other two catalysts.

3.6 H₂-TPR analysis

The H₂-TPR profiles of the 30%Ni/SBA-15, 1%Pt–30%Ni/SBA-15 and 2%Pt–30%Ni/SBA-15 catalysts (Fig. 5) were also recorded to examine the reducibility of the fresh catalysts. The peak observed at 390 °C in the profile of 30%Ni/SBA-15 corresponded to the reduction of large size NiO particles,

**Fig. 4** TEM images of **a** SBA-15, **b** 30%Ni/SBA-15, **c** 1%Pt–30%Ni/SBA-15 and **d** 2%Pt–30%Ni/SBA-15

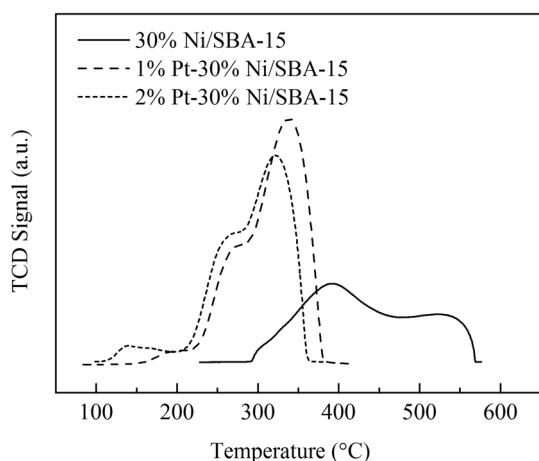


Fig. 5 H₂-TPR profiles of the prepared catalysts

because the large size particles aggregate on the surface of SBA-15 and were easily reduced. The second peak at 540 °C was attributed to the reduction of small NiO particles, because the particles with small particle size entered the channels of SBA-15, and the reduction temperature rose due to the limitation of the pores [13].

The addition of Pt shifted the reduction peaks of the 30%Ni/SBA-15 catalyst to lower temperatures. More specifically, a broad reduction peak from 200 to 380 °C was observed for 1%Pt–30%Ni/SBA-15 and 2%Pt–30%Ni/SBA-15, with two maxima at 261 and 340 °C and at 255 and 317 °C, respectively (Fig. 5). These results suggested that the reduction temperature of the catalysts decreased as the amount of loaded Pt increased, which could be attributed to the H₂ spillover effect [16]. Hydrogen in the reduction process contacts with active Pt and dissociates to produce active hydrogen, and the active hydrogen can reduce the nearby NiO phase during the migration process.

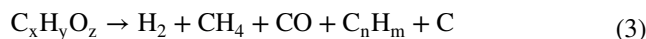
The appearance of an additional reduction peak in the low temperature range (~150 °C) in the H₂-TPR profiles of both Pt-loaded catalysts also confirmed that the addition of metallic Pt favoured a more uniform dispersion of the NiO phase on the support surface. Researchers also reported that the reduction performance of the catalyst is affected by the interaction between the metal and the support [17]. Here, the reduction peak observed for 2%Pt–30%Ni/SBA-15 at a lower temperature suggested that the interaction between the metal particles and the support was weak, thus facilitating the reduction of the oxides and increasing the catalyst activity.

3.7 Catalytic cracking of WCOMC

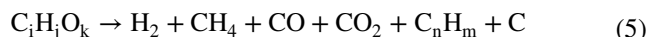
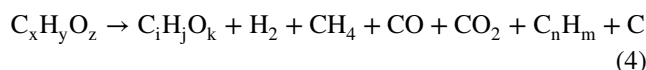
3.7.1 WCOMC cracking

In our previous work, we studied the WCOMC cracking without using a catalyst, revealing that it is an endothermic

process and that the H₂ content in the gas products increases with increasing temperature [9]. As also shown in Eq. (3), the WCOMC can be completely decomposed at high temperatures, leading to the generation of small gas molecules and solid carbon, while no liquid is produced.



However, along with the gas and solid molecules [Eq. (4)], an incomplete decomposition of the WCOMC during the cracking process leads to the generation of liquid products (C_iH_jO_k), which can decompose into smaller molecules, as shown in Eq. (5).



During the cracking process, reactions between the products, i.e. CH₄ reforming [Eqs. (6, 7)], water–gas shift [Eq. (8)], carbon gasification [Eqs. (9, 10)], methanation [Eqs. (11, 12)] and the Boudouard reaction [Eq. (13)] may also occur.



3.7.2 Effect of catalyst type on gas product distribution

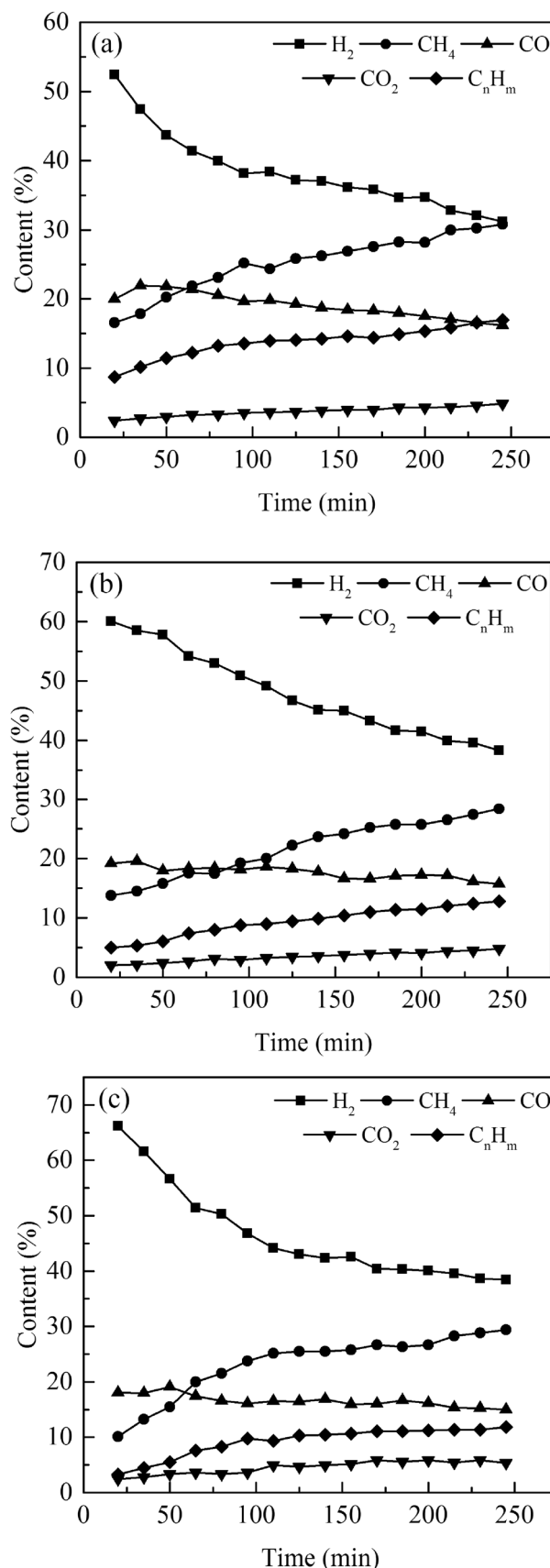
In order to examine the effect of the 30%Ni/SBA-15 and Pt-loaded 30%Ni/SBA-15 catalysts on the distribution of gas products, the catalytic cracking of the WCOMC [Eq. (3)] was performed using a liquid feed flow rate of 0.02 mL min⁻¹ and a reaction temperature of 750 °C. Among the three catalysts, 2%Pt–30%Ni/SBA-15 showed the highest activity, leading to a H₂ content of ~66.2 vol% in the first 20 min of the reaction (Fig. 6c). However, over time, the H₂ content in the gas product gradually decreased from 66.2 to 38.5 vol%, indicating that the catalytic activity

Fig. 6 Effect of the **a** 30%Ni/SBA-15, **b** 1%Pt–30%Ni/SBA-15 and **c** 2%Pt–30%Ni/SBA-15 catalysts on the content of each gas product at a reaction temperature of 750 °C

also decreased over time due to the sintering of the catalyst and the increase in the amount of surface carbon. In contrast, the H₂ content decreased from 52.4 to 31.2 vol% when 30%Ni/SBA-15 was used, indicating that the addition of Pt can effectively improve the catalyst performance in the H₂ production from the WCOMC (Fig. 6a). Moreover, the use of 1% Pt led to a slightly lower initial H₂ content (60.1 vol%) compared to 2%Pt–30%Ni/SBA-15, which decreased to 38.2 vol% after 250 min (Fig. 6b), suggesting that a higher Pt content can also improve the catalytic activity. Nevertheless, extending the reaction time favoured the generation of CO₂ and CH₄ and reduced the content of CO regardless of the catalyst, which could be attributed to the promotion of the water–gas shift, methanation and Boudouard reactions [Eqs. (8, 11, 12, 13)].

The favouring effect of the Pt addition was also confirmed by comparing the current results with the results of our previous study [9]. Specifically, we found that the 50%Ni/SBA-15 catalyst exhibits excellent catalytic activity, leading to a H₂ content in the gas product of 69.0 vol%, which decreased to 36.3 vol% after 4 h. Although this Ni-based monometallic catalyst with a high metal content showed higher catalytic activity in the initial reaction stage than the 2%Pt–30%Ni/SBA-15 catalyst developed in the present work, 50%Ni/SBA-15 exhibited lower stability. Araiza et al. prepared Pt–Ni/CeO₂ catalyst for dry reforming of methane to produce hydrogen. The results showed that the addition of Pt improved the activity of the catalyst. At 650 °C, the conversion rate of CH₄ was only about 30% by using Ni/CeO₂ catalyst, while 53% of conversion rate could be obtained by using Pt–Ni/CeO₂ catalyst [18]. Pudukudy et al. also studied the Pd doping Ni/SBA-15 to promote methane decomposition. The results showed that the addition of Pd improved the dispersion of NiO on the SBA-15 and reduced the reduction temperature of the catalyst, thus improving the catalytic activity and stability of the catalyst. At 700 °C, the maximum hydrogen yield of 0.4%Pd–50%Ni/SBA-15 was 59%, and after 420 min, the hydrogen production rate remained at about 46%. The highest hydrogen production rate on 50%Ni/SBA-15 was about 50%, and after 420 min decreased to 39% [7]. Therefore, although the total metal content in 2%Pt–30%Ni/SBA-15 was lower compared to 50%Ni/SBA-15, we concluded that the addition of Pt can significantly improve the catalyst stability and favour its application in practice.

The higher catalytic activity of the Pt-loaded catalysts compared to the Pt-free catalyst could also be related to the modification of the surface structure of Ni⁰ and the regulation of the d-electron structure. Researchers reported that



the concentration of Ni in catalysts with a small Pt amount is much higher than that of Pt [19]. Moreover, the existence of a Pt–Ni alloy may electronically and geometrically change the surface structure of Ni⁰ and tune the d-electron structure, thereby affecting the catalytic performance. In addition, earlier studies suggested that the electron transfer between Ni and Pt can change the electronic structure of Pt, making it slightly negative, thus reducing the density of Fermi level states and subsequently increasing the catalytic activity [20, 21].

Furthermore, the higher catalytic performance of 2%Pt–30%Ni/SBA-15 could be attributed to its excellent morphological and structural characteristics. BET studies showed that 2%Pt–30%Ni/SBA-15 exhibits a larger specific surface area and pore volume and a more easily reducible oxide phase compared to the other two examined catalysts. These results were consistent with previous studies, which supported that the addition of an active metal can promote the dispersion of active metal particles on the support surface [22], thereby explaining the high catalytic performance of catalysts loaded with active metals. In addition, the H₂-TPR studies confirmed that a weaker interaction was developed between the metal oxide and the support, which facilitated the reduction of the metal oxide to a metallic state and increased the catalytic activity in cracking reactions. The results of Pudukudy et al. also confirmed that the surface area of the catalyst increased from 22.6 to 29.3 m² g⁻¹ when Pd was added to catalyst Ni/MgAl₂O₄. In addition, the dispersion of NiO on the surface of the magnesium alminate was improved. At the reaction temperature of 700 °C, the highest H₂ yield of the catalyst doped with Pd could reach 57%, while the highest H₂ yield of the catalyst without Pd was only 49%. After 425 min, the hydrogen production rate of the catalyst doped with Pd (about 30%) was still higher than that of the catalyst without Pd (about 20%) [23].

3.7.3 Effect of reaction temperature on the gas product distribution

To examine the effect of the reaction temperature on product distribution, the composition and content of the gas products using 2%Pt–30%Ni/SBA-15 were also evaluated at different cracking temperatures. The highest H₂ content (66.2 vol%) was obtained at 750 °C, and no rapid catalyst deactivation was observed at this temperature. However, a lower catalytic activity and faster deactivation rate was observed at 650 °C (Fig. 7a). This difference could be due to the incomplete WCOMC cracking at lower temperatures, which promoted the coverage of the catalyst surface with incompletely decomposed liquid molecules. In contrast, when the temperature was raised to 800–850 °C, the H₂ content decreased due to the catalyst sintering (Fig. 7c, d).

In addition, we observed that the content of CH₄ gradually increased with increasing temperature (Fig. 7a–d). During cracking, the decarbonylation and decarboxylation of triacylglycerol leads to the formation of intermediate and light hydrocarbons, followed by the generation of CH₄ via a β-scission reaction [24]. However, this process requires a high activation energy, which can only be provided by heating at a high temperature. In contrast to CH₄, the temperature changes only slightly affected the content of CO and CO₂. According to literature, the cracking of triglycerides produces heavy oxygenated hydrocarbons, and the decarbonylation and decarboxylation caused by the cleavage of unsaturated bonds can generate CO and CO₂ [25]. Moreover, the increasing temperature favoured the C_nH_m cracking, as its content was lower with increasing temperature from 650 to 850 °C.

Although temperature plays a leading role in the gas composition and the content of WCOMC cracking products, competitive side reactions can also affect the product distribution. As earlier mentioned, the carbon gasification [Eq. (9)] and Boudouard [Eq. (13)] reactions can increase the CO content, whereas the water–gas shift reaction [Eq. (8)] can increase content of CO₂.

3.8 SEM analysis of deposited CNTs

The morphology of carbon atoms deposited on the catalyst surface during the cracking process is particularly important, as solid carbon can reduce the formation of CO_x, thereby reducing greenhouse gas emissions. Therefore, here, the external morphology of CNTs deposited on the surface of the prepared catalysts during WCOMC cracking at 750 °C was analysed by SEM. Based on the recorded SEM images (Fig. 8a–c), the surface of the different catalysts was covered with a large number of CNTs entangled with each other. However, due to the different growth directions, their length could not be estimated. Metal particles were also observed on the CNT wall and on the top of each tube. Compared to 30%Ni/SBA-15, the surface of the Pt-loaded catalysts was more densely covered by CNTs, which was consistent with the higher activity of 1%Pt–30%Ni/SBA-15 and 2%Pt–30%Ni/SBA-15 [22], as the addition of Pt increased the catalytic activity and promoted the WCOMC cracking, leading to the deposition of more CNTs on the catalyst surface.

The effect of the reaction temperature on the deposition of CNTs on the 2%Pt–30%Ni/SBA-15 surface was also examined by SEM, as the temperature can affect the cracking rate of raw materials and the formation rate of carbon deposits. Here, we observed that at low temperatures, the rate of WCOMC cracking and the formation rate of CNTs were not balanced. In particular, at 650 °C, a considerable number of carbon atoms were wrapped on the catalyst surface in an

Fig. 7 Distribution of gas products obtained during WCOMC cracking catalysed by 2%Pt–30%Ni/SBA-15 at **a** 650 °C, **b** 700 °C, **c** 800 °C and **d** 850 °C

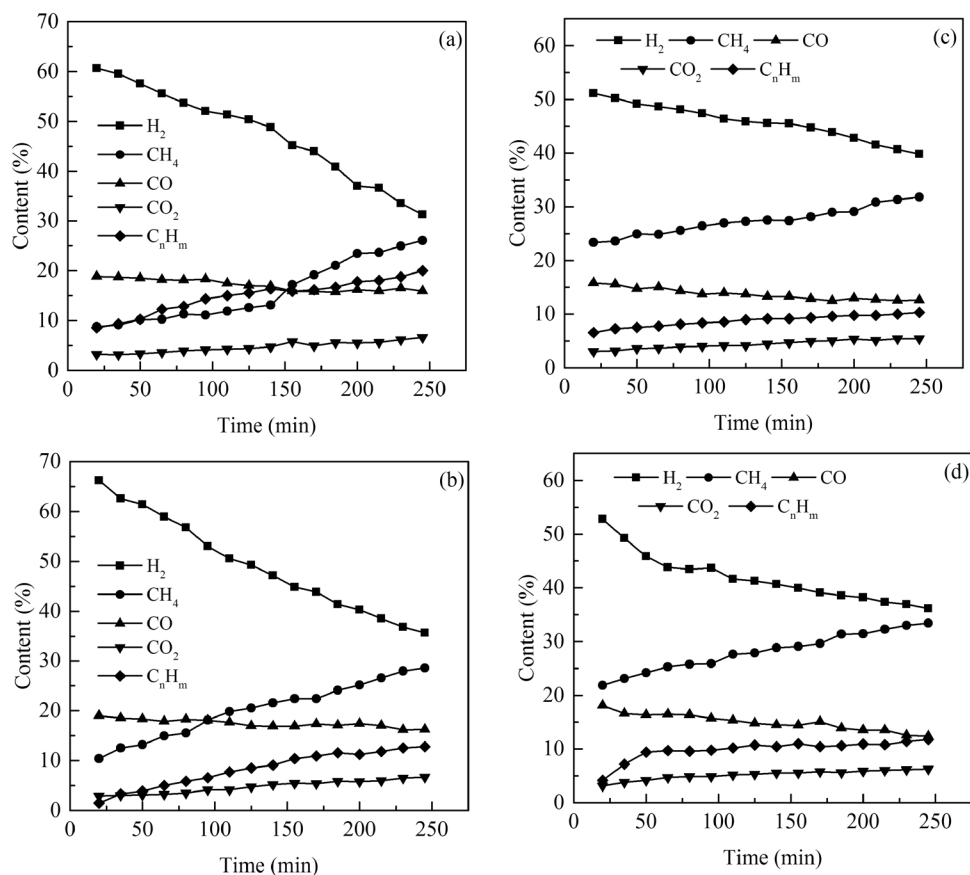
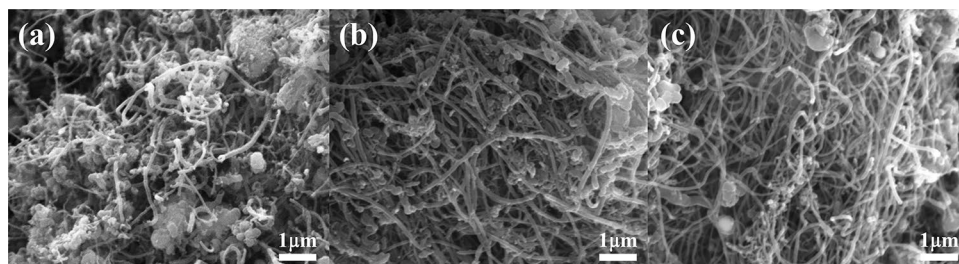


Fig. 8 SEM images of CNTs deposited on the surface of **a** 30%Ni/SBA-15, **b** 1%Pt–30%Ni/SBA-15 and **c** 2%Pt–30%Ni/SBA-15 catalysts during WCOMC cracking at 750 °C



amorphous state, as the catalytic activity was low and the WCOMC cracking was insufficient, leading to the deposition of a small amount of carbon atoms on the catalyst surface (Fig. 9a).

In addition, we observed that temperatures above 700 °C led to the formation of thinner CNTs (Fig. 9c, d). This could be explained by the fact that the effect of temperature on the diameter of CNTs is related to the morphology of metal particles [26]. At low temperatures, metal particles attach to the top or inside the carrier pores in solid form, whereas at high temperatures, they turn into a quasi-liquid state and exhibit mobility. The same phase transition has also been observed during cracking reactions [27, 28]. This phenomenon can be explained by the Lindemann effect, where heating of metal particles to temperatures lower than their melting point leads

to a reduction of their size from the original size range to the nm scale and to a reduction in the melting point [29]. For instance, the melting point of metallic Ni is 1455 °C, but when Ni nanoparticles are heated to 500 °C, they turn into molten and softened particles, leading to a quasi-liquid state. Consequently, in this study, thinner CNTs were formed as the temperature increased due to the higher diffusion rate of the carbon atoms generated by WCOMC cracking inside the quasi-liquid catalyst compared to that inside the solid catalyst.

3.9 TEM analysis of deposited CNTs

The internal structure of the CNTs deposited on the different Ni-based catalysts at 750 °C was studied by TEM.

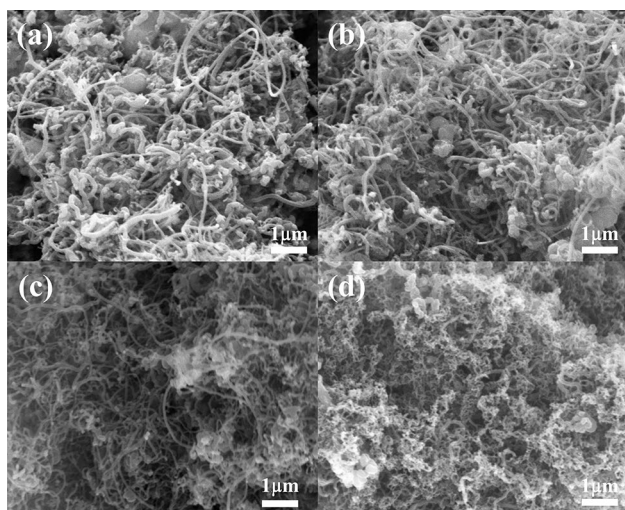


Fig. 9 SEM images of CNTs deposited over 2%Pt–30%Ni/SBA-15 during WCOMC cracking at **a** 650 °C, **b** 700 °C, **c** 800 °C and **d** 850 °C

As shown in Fig. 10, the diameters of the carbon products ranged mainly between 20 and 100 nm. Metal particles were also observed on the CNTs wall and on the top of each tube. The formation mechanism of CNTs could be explained by diffusion precipitation mechanism: gas-phase hydrocarbon decomposed on the active metal site to form C atom and the C atom diffused through Ni particle to precipitate at the bottom of the metal to form CNTs. The CNTs pushed the metal particle upward until the metal was covered with carbon and deactivated, and finally CNTs stopped growing [30, 31]. Thus, a small catalyst amount could adhere to the CNTs passing through the catalyst during the growth process. Moreover, among all catalysts, the thinnest CNTs were formed on 2%Pt–30%Ni/SBA-15 and were related to broken or molten catalyst particles (Fig. 10e, f). In contrast, bamboo-shaped CNTs were observed on the 1%Pt–30%Ni/SBA-15 catalyst with a non-continuous inner hollow (Fig. 10g, h). Due to the strong interaction between the catalyst particles and the catalyst support, the shape of these CNTs indicated their conversion from nanotubes to nanofibers [32, 33]. This morphological change of the deposited carbon nanomaterials during the growth process was further confirmed from the TEM images in Fig. 10c, d, where the internal characteristics of the collected carbon nanomaterials were similar to those of nanofibers.

3.10 TGA analysis

The TGA method was used to analyse the oxidation stability and yield of the CNTs collected after the cracking of the WCOMC over the Ni-based catalysts. The TGA profiles

showed a significant weight loss above 500 °C (Fig. 11), which was attributed to the pyrolytic oxidation of the deposited carbon materials. Since, the oxidation of amorphous carbon materials occurs before 400 °C [34], the profiles also indicated that the deposited carbon materials did not include amorphous carbon and exhibited high oxidation stability. Moreover, the CNT yields on 30%Ni/SBA-15, 1%Pt–30%Ni/SBA-15 and 2%Pt–30%Ni/SBA-15 were 894%, 902% and 917%, respectively, suggesting that the high catalytic activity due to the addition of metallic Pt increased the amount of carbon atoms and in turn the yield of CNTs deposited during WCOMC cracking [35, 36].

3.11 XRD analysis of spent catalysts

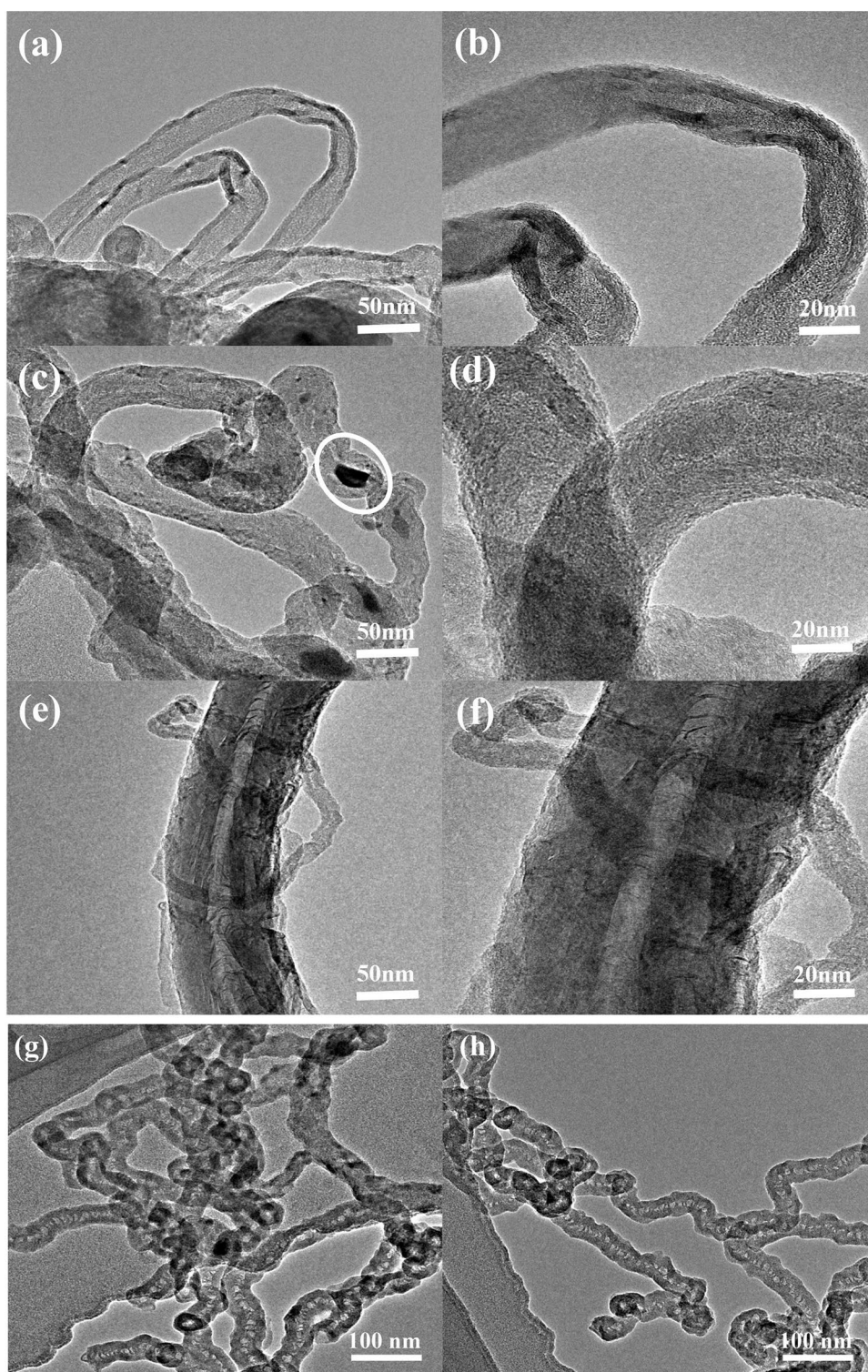
The XRD patterns of the catalysts collected after the cracking process at 750 °C were also recorded to identify the crystalline phases on the spent catalysts. The diffraction peaks at $\sim 26.4^\circ$, 54.5° and 77.8° observed for all catalysts were attributed to the carbon deposited on the catalysts (Fig. 12). Specifically, the diffraction peak corresponding to the (002) plane indicated that the deposited carbon exhibits a graphite crystal structure [37, 38], while the diffraction peaks at 44.2° , 51.8° and 76.3° were attributed to the metallic phase of Ni. In addition, no diffraction peak of NiO was detected, suggesting that it has been completely reduced to its metal form in the catalyst reduction stage [39]. The remaining weak peaks corresponded to the formation of metal carbides (NiC).

Researchers also reported that the carbon diffraction peak on the (002) plane indicates the degree of crystallinity and graphitisation of the nanocarbons deposited on a catalyst [40, 41]. Here, the intensity of the diffraction peaks increased with the addition of Pt (Fig. 12), implying that the crystallinity of deposited carbon also increased. However, the diffraction peak of Ni could also be detected in the XRD patterns, because the reaction product was collected as a mixture with a large catalyst amount that was not completely inactive.

3.12 Raman spectroscopic analysis of deposited CNTs

The graphitisation and presence of defects in the deposited CNTs were determined by Raman analysis. The D band detected at $\sim 1350\text{ cm}^{-1}$ in all Raman spectra was attributed to defects on the graphite sheet and amorphous carbon, while the G band at $\sim 1580\text{ cm}^{-1}$ was correlated with the stretching vibration of the C–C bond between graphite sheets (Fig. 13) [42]. The intensity ratio (I_D/I_G) could also be used to estimate the graphitisation and crystallisation index of CNTs [43], as small ratios would indicate a high degree of graphitisation and crystallinity. The I_D/I_G value

Fig. 10 TEM images of CNTs deposited over **a, b** 30%Ni/SBA-15, **c, d, g, h** 1%Pt–30%Ni/SBA-15 and **e, f** 2%Pt–30%Ni/SBA-15



of the CNTs obtained on the 2%Pt–30%Ni/SBA-15 catalyst was 0.47 (Fig. 13c), suggesting that the CNTs exhibited few defects and high crystallinity. These results were also consistent with the XRD findings obtained for 2%Pt–30%Ni/SBA-15 after the reaction. Also, a 2D peak was detected at $\sim 2700\text{ cm}^{-1}$ and was attributed to the second-order

two-phonon process in CNTs. It is also known that the intensity ratio of the 2D to the G peak (I_{2D}/I_G) reflects the purity and graphite layer quality of CNTs [44, 45]. The current Raman analysis revealed that the I_{2D}/I_G value was the highest for the CNTs obtained on the 2%Pt–30%Ni/SBA-15 catalyst,

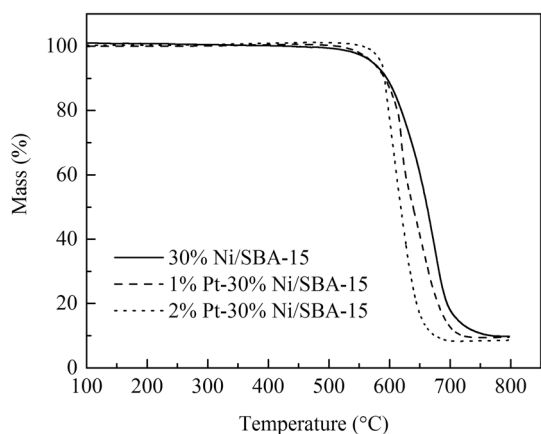


Fig. 11 TGA profiles of CNTs deposited on 30%Ni/SBA-15, 1%Pt-30%Ni/SBA-15 and 2%Pt-30%Ni/SBA-15

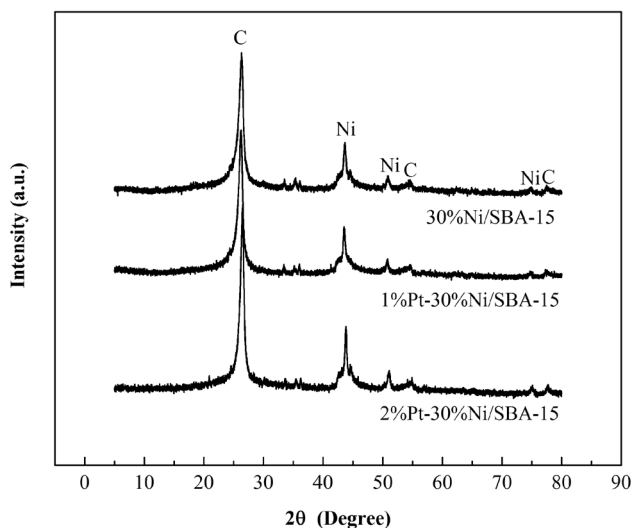


Fig. 12 XRD patterns of the catalysts collected after the reaction at 750 °C

indicating that the corresponding CNTs had the highest purity and the best graphite layer quality.

4 Conclusions

H₂ production from fossil fuels attracted particular interest in the last decades. However, the utilisation of fossil fuel resources in large amounts for H₂ production begun to cause serious energy and environmental problems. In order to limit the consumption of fossil fuels, researchers focused on WCO, which is a cheap and abundant raw material that consists of elemental hydrogen and carbon and could be an ideal substitute for fossil fuels. To that end, a limited number of studies already investigated the catalytic cracking of WCO

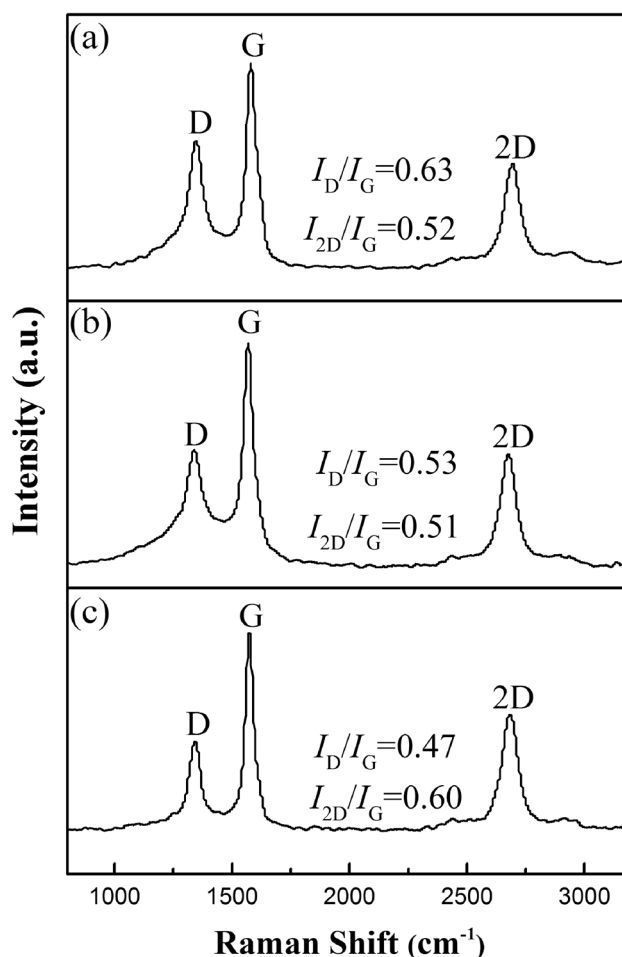


Fig. 13 Raman spectra of the CNTs deposited on a 30%Ni/SBA-15, b 1%Pt-30%Ni/SBA-15 and c 2%Pt-30%Ni/SBA-15

to produce H₂ and high value-added carbon materials. In this study, to catalyse the cracking of a WCOMC for the production of H₂ and CNTs, we developed Pt–Ni/SBA-15 catalysts with a Pt content of 0–2%. Among them, 2%Pt-30%Ni/SBA-15 showed the best catalytic activity and stability at 750 °C, affording a H₂ content of 66.2 vol%. The excellent catalytic performance of 2%Pt-30%Ni/SBA-15 compared to the other two catalysts was attributed to its larger specific surface area and pore volume and its more easily reducible oxide phase. In addition, we demonstrated that CNTs with high crystallinity, oxidation stability, graphitisation and purity could be successfully formed during this process.

Acknowledgements This study was funded by the National Natural Science Foundation of Ningxia (Grant No. 2020AAC02027), China; the National Natural Science Foundation of China (Grant No. 21962001), China; the Ningxia Scientific and Technological Innovation Leading Personnel Training (Grant No. KJT2017006), China; the talent highland of research and development of high-value utilization technology of low-quality resources in Ningxia, China are gratefully acknowledged.

Author contributions WL: Writing–reviewing and editing, specifically performing the experiments, data collection and analysis. GZ: Specifically performing the experiments, data collection and analysis. SH: Data collection and analysis. HY: Conceptualization and methodology. WH: Material preparation.

Data availability All data generated or analysed during this study are included in this published article.

Declarations

Conflict of interest All authors certify that they have no affiliations with or involvement in any organization or entity with any financial interest or non-financial interest in the subject matter or materials discussed in this manuscript.

References

- J. Chi, H. Yu, Chin. J. Catal. **39**(3), 390–394 (2018)
- Y. Lei, C. Yang, J. Hou, F. Wang, S. Min, X. Ma, Z. Jin, J. Xu, G. Lu, K.-W. Huang, Appl. Catal. B **216**, 59–69 (2017)
- P. Nikolaidis, A. Poullikkas, Renew. Sustain. Energy Rev. **67**, 597–611 (2017)
- D. Torres, J. Pinilla, I. Suelves, Appl. Catal. A **559**, 10–19 (2018)
- S. Zhou, Y. Wei, S. Zhang, B. Li, H. Wang, Y. Yang, M. Barati, J. Cleaner. Prod. **236**, 117668 (2019)
- M. Pudukudy, Z. Yaakob, Q. Jia, M.S. Takriff, New J. Chem. **42**(18), 14843–14856 (2018)
- M. Pudukudy, Z. Yaakob, Z.S. Akmal, Appl. Surf. Sci. **353**, 127–136 (2015)
- G.D.B. Nuernberg, H.V. Fajardo, E.L. Foletto, S.M. Hickel-Probst, N.L. Carreño, L.F. Probst, J. Barrault, Catal. Today **176**(1), 465–469 (2011)
- W. Liu, H. Yuan, Int. J. Energy Res. **44**(14), 11564–11582 (2020)
- D. Zhao, Q. Huo, J. Feng, B.F. Chmelka, G.D. Stucky, J. Am. Chem. Soc. **120**(24), 6024–6036 (1998)
- N. Anand, P. Ramudu, K.H.P. Reddy, K.S.R. Rao, B. Jagadeesh, V.S.P. Babu, D.R. Burri, Appl. Catal. A **454**, 119–126 (2013)
- W. Chen, Z. Xie, H. Liang, X. Zhou, W. Hu, X. Shu, RSC Adv. **10**(6), 3175–3183 (2020)
- S. He, S. He, L. Zhang, X. Li, J. Wang, D. He, J. Lu, Y. Luo, Catal. Today **258**, 162–168 (2015)
- C. Crisafulli, S. Scirè, S. Minicò, L. Solarino, Appl. Catal. A **225**(1–2), 1–9 (2002)
- X. Cai, R. Lin, D.D. Shen, Y. Zhu, ACS Appl. Mater. Inter. **11**(33), 1–17 (2019)
- H. Sharma, A. Dhir, Fuel **279**, 118389 (2020)
- A. Rategarpanah, F. Meshkani, Y. Wang, H. Arandiyan, M. Rezaei, Energy Convers. Manag. **166**, 268–280 (2018)
- D.G. Araiza, D.G. Arcos, A. Gomez, G. Díaz, Catal. Today **360**(5), 46 (2021). <https://doi.org/10.1016/j.cattod.2019.06.018>
- L. Zhou, M. Harb, M.N. Hedhili, N. Al Mana, J.M. Basset, RSC Adv. **7**(7), 4078–4082 (2017)
- Y. Yan, Y. Zhang, T. Jiang, T. Xiao, P.P. Edwards, F. Cao, RSC Adv. **7**(61), 38251–38256 (2017)
- L. Li, Y. Wu, J. Lu, C. Nan, Y. Li, Chem. Comm. **49**(68), 7486–7488 (2013)
- S. Takenaka, Y. Shigeta, E. Tanabe, K. Otsuka, J. Phys. Chem. B **108**(23), 7656–7664 (2004)
- M. Pudukudy, Z. Yaakob, M.S. Takriff, Appl. Surf. Sci. **356**, 1320–1326 (2015)
- I. Shimada, S. Kato, N. Hirazawa, Y. Nakamura, H. Ohta, K. Suzuki, T. Takatsuka, Ind. Eng. Chem. Res. **56**(1), 75–86 (2017)
- V. R. Wiggers, R. F. Beims, L. Ender, E. L. Simionatto, H. F. Meier, (Inech Open Ltd., London, 2017)
- V. Parmon, Catal. Lett. **42**(3–4), 195–199 (1996)
- S. Pinjari, M.K. Kumaravelan, V.C. Peddy, S. Gandham, J. Patruni, S. Velluru, P. Kumar, Int. J. Hydrog. Energy **43**(5), 2781–2793 (2018)
- D. Chen, K.O. Christensen, E. Ochoa-Fernández, Z. Yu, B. Tøtdal, N. Latorre, A. Monzón, A. Holmen, J. Catal. **229**(1), 82–96 (2005)
- B. Michalkiewicz, J. Majewska, Int. J. Hydrog. Energy **39**(9), 4691–4697 (2014)
- B.M. Al-Swai, N. Osman, M.S. Alnarabiji, A.A. Adesina, B. Abdullah, Ind. Eng. Chem. Res. **58**(2), 539–552 (2018)
- R.T.K. Baker, P.S. Harris, R.B. Thomas, R.J. Waite, J. Catal. **30**(1), 86–95 (1973)
- J. Pinilla, R. Utrilla, R. Karn, I. Suelves, M. Lázaro, R. Moliner, A. García, J. Rouzaud, Int. J. Hydrog. Energy **36**(13), 7832–7843 (2011)
- S. Shokry, A. El Morsi, M. Sabaa, R. Mohamed, H. El Sorogy, Egypt. J. Pet. **23**(2), 183–189 (2014)
- A.E. Awadallah, A.A. Aboul-Enein, A.K. Aboul-Gheit, Energy Convers. Manag. **77**, 143–151 (2014)
- M. Pudukudy, Z. Yaakob, M.S. Takriff, Energy Convers. Manag. **126**, 302–315 (2016)
- X. Yin, L. He, S.S.A. Syed-Hassan, W. Deng, P. Ling, Y. Xiong, X. Hu, S. Su, S. Hu, Y. Wang, Fuel **280**, 118601 (2020)
- A. Awadallah, A. Aboul-Enein, D. El-Desouki, A. Aboul-Gheit, Appl. Surf. Sci. **296**, 100–107 (2014)
- S. Kawasaki, Y. Matsuoka, T. Yokomae, Y. Nojima, F. Okino, H. Touhara, H. Kataura, Carbon **43**(1), 37–45 (2005)
- M. Pudukudy, A. Kadier, Z. Yaakob, M.S. Takriff, Int. J. Hydrog. Energy **41**(41), 18509–18521 (2016)
- A. Awadallah, W. Ahmed, M.N. El-Din, A. Aboul-Enein, Appl. Surf. Sci. **287**, 415–422 (2013)
- A.S. Al Fatesh, S.O. Kasim, A.A. Ibrahim, A.S. Al-Awadi, A.E. Abasaheed, A.H. Fakeeha, A.E. Awadallah, Renew. Energy **155**, 969 (2020). <https://doi.org/10.1016/j.renene.2020.04.038>
- J. Gong, J. Liu, Z. Jiang, X. Chen, X. Wen, E. Mijowska, T. Tang, Appl. Catal. B **152**, 289–299 (2014)
- D. Yao, C. Wu, H. Yang, Y. Zhang, M.A. Nahil, Y. Chen, P.T. Williams, H. Chen, Energy Convers. Manag. **148**, 692–700 (2017)
- T. Batakliiev, I. Petrova-Doycheva, V. Angelov, V. Georgiev, E. Ivanov, R. Kotsilkova, M. Casa, C. Cirillo, R. Adami, M. Sarno, Appl. Sci. **9**(3), 469 (2019)
- D. Yao, Y. Zhang, P.T. Williams, H. Yang, H. Chen, Appl. Catal. B **221**, 584–597 (2018)

Publisher's Note Springer Nature remains neutral with regard to jurisdictional claims in published maps and institutional affiliations.